Applied Energy 210 (2018) 327–338

Contents lists available at ScienceDirect

Applied Energy

journal homepage: www.elsevier.com/locate/apenergy

A dynamic model for thermoelectric generator applied to vehicle waste heat recovery

Song Lan, Zhijia Yang, Rui Chen*, Richard Stobart

Department of Aeronautical and Automotive Engineering, Loughborough University, LE11 3TU, UK

HIGHLIGHTS

- Developed a dynamic model of TEG system designed for vehicle waste heat recovery.
- Experimental validations are performed on both a TEM test rig and a TEG engine test bench.
- The model can be used as a basis for a model-based control design.
- The integration of TEMs with the HXRs is important for the overall power output.

ARTICLE INFO

Keywords:
Module-based
Dynamic model
Thermoelectric generator
Automotive waste heat recovery

ABSTRACT

Waste heat recovery using a thermoelectric generator (TEG) is a promising approach for vehicle original equipment manufacturers to reduce fuel consumption and lower CO_2 emissions. A TEG can convert otherwise wasted thermal energy from engines to electricity directly for use in the vehicle systems. This paper focuses on the development of a dynamic model of TEG system designed for vehicle waste heat recovery, which is made up of counter-flow heat exchangers (HXRs) and commercial thermoelectric modules (TEMs). The model is built from thermoelectric materials into a TEM and then into a TEG system. Compared to other TEG models, the tuning and validation process of the proposed model is more complete. Experiments are done on both a TEM test rig and a heavy-duty diesel engine, which is equipped with a prototype TEG on the exhaust gas recirculation (EGR) path. Simulations of steady-state operating points as well as the response to typical engine cycle test show good agreement with experimental data.

A TEG installed upstream of the after-treatment system in a heavy-duty truck has been modelled to predict the temperatures and power output in a dynamic driving cycle. The simulation results of temperatures show the model can be used as a basis to develop a control system for dynamic operation to ensure safety operation of TEG and efficient operation of the after-treatment system. A comparison of power output of the systems under different scenarios underlines the importance of integration of TEM with HXRs. Based on the simulation results, around 20% average power output increase can be expected by optimizing the thermal contact conductance and the heat transfer coefficient of hot side HXR.

1. Introduction

Driven by CO_2 legislation and fuel cost, car original equipment manufacturers have emphasised the efficiency of the engine and drivetrain. For the typical energy flow path of an internal combustion engine (ICE), approximately one third of the energy is discharged by exhaust gas. Interest in waste-heat recovery (WHR) has flourished in recent years [1–4]. Thermoelectric generator (TEG), as one of the WHR methods, has attracted substantial interest because of its advantages of silent operation and compactness. The performance of current TEG systems is largely decided by the thermoelectric modules (TEMs). Significant strides have been made in the materials of TEMs and recent work is beginning to translate those material improvements into TEG performance [4].

In the development of TEG for WHR, a number of modelling studies have been carried out to evaluate the performance [3,5–9] and optimize the design parameters [10–13]. However, only a few of studies [8,6,12,13,9] took the dynamics of the WHR systerm into account. In fact, the transient performance of TEG is important, especially in the application of vehicle WHR. First of all, the exhaust heat flow is often changeable during a normal operation of the car where start-up, shutdown, and engine load changes are a major concern. Yu et al. [8]

* Corresponding author.
E-mail address: r.chen@lboro.ac.uk (R. Chen).

https://doi.org/10.1016/j.apenergy.2017.11.004
Received 26 June 2017; Received in revised form 25 September 2017; Accepted 1 November 2017

Nomenclature

Abbreviation

DOC	diesel oxidation catalyst
DPF	catalyst-diesel particulate filter
HXR	heat exchanger
ICE	internal combustion engine
MAE	mean absolute error
NRTC	non-road transient cycle
Nu	Nusselt number
Pr	Prandtl Number
Re	Reynolds number
TEG	thermoelectric generator
TEM	thermoelectric module
WHR	waste-heat recovery

Subscripts

ap	aluminium plate
cd	cold end
col	coolant
cp	ceramic plate
ct	contact
cxr	cold side heat exchanger
exh	exhaust gas
gap	air gap
hd	hot end
hxr	hot side heat exchanger
in	gas-in & coolant-in
load	electrical load
n	n-type thermoelectric element
ocv	open circulate
out	output & gas-out & coolant-out
p	p-type thermoelectric element
tc	thermocouples

Symbols

$\dot{m}$	flow rate, kg/s
σ	electric conductivity, S/m
A	area, m^2
b	tuning constant
c	specific heat capacity, J/(kg K)
D	hydraulic diameter, m
F	clamping force, N
h	heat transfer coefficient, W/(m^2 K)
I	current, A
K	thermal conductance, W/K
k	thermal conductivity, W/(m K)
l	length, m
M	mass, kg
n	number
P	power, W
Q	heat flow rate, W
R	electrical resistance, Ω
S	Seebeck coefficient, V/K
T	temperature, K
U	voltage, V

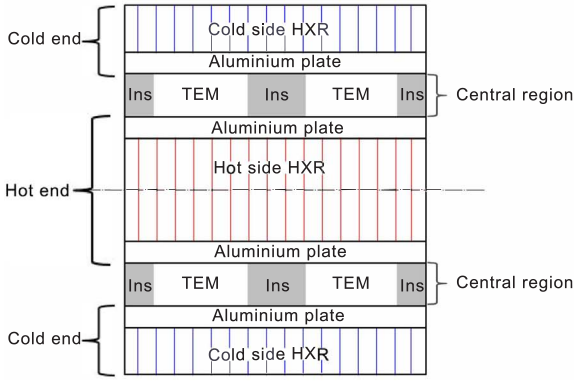

(a) Front view of a TEG system.

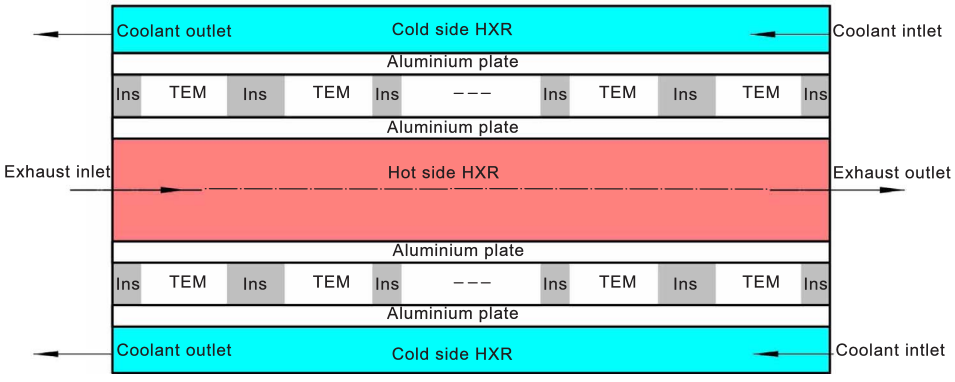

(b) Side view of a TEG system.

Fig. 1. Structure of a TEG system.

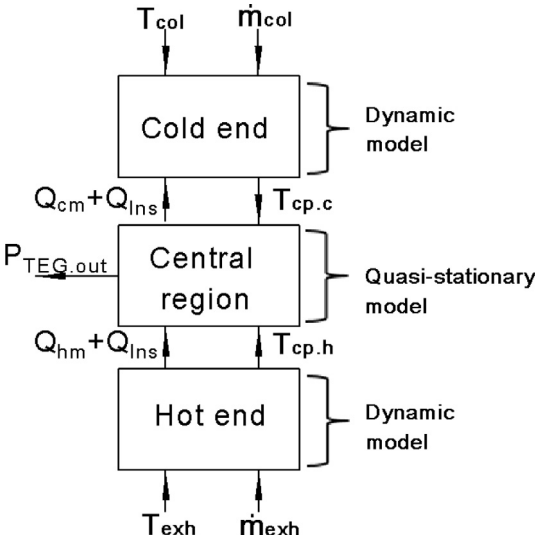

Fig. 2. Structure and parameters of the model.

developed a dynamic numerical model of TEG WHR model and found that the changing vehicle speed was a critical factor affecting the TEG performance and increased vehicle speed led to a fast response and better performance of TEG. He et al. [13] found that increase in exhaust temperature led to an increase in the optimal length and reduction in the optimal width based on a dynamic optimization simulation. Secondly, the highly temperature dependent characteristic of the thermoelectric properties also underlines the importance of dynamic operation of the TEG system. The simulation results presented by Meng et al. [12] showed that the temperature dependence of thermoelectric properties had a significant effect on the power, efficiency and optimal variables of TEG. Thirdly, the temperature of the cold end of the TEG, which is usually integrated with engine coolant is also often changed with the flow rate of cooling unit and operation of radiator. Gou et al. [6] investigated the dynamic characteristics of TEG using a theoretical dynamic model and found out that enhancing heat dissipation on the cold side could lead to a greater improvement on TEG performance than enhancing heat transfer on hot side. Meng et al. [9] studied the transient behaviour of the TEG when cold end temperature changed. The response hysteresis of the output power to the cold end temperature was observed. The conversion efficiency of TEG was found to overshoot and undershoot respectively in the decreasing and increasing cases of cold end temperature.

Based on previous studies [8,6,12,13,9] for the transient behaviour of TEG, more reliable performance prediction and appropriate optimization guidance has emerged. However, an important function for a dynamic TEG model to enable safe operation of the TEG system and effective operation of aftertreatment system has been neglected. The maximum temperature limit for the most popular bismuth tellurium module is 250 °C [14] while the exhaust temperature of a diesel engine and a gasoline engine can be respectively higher than 400 °C and 800 °C. Besides, when the TEG is integrated upstream of after-treatment system, the outlet temperature of TEG can affect the catalytic conversion [15].

Therefore, a dynamic TEG model is needed to capture both the dynamics of the temperatures for the hot end and outlet exhaust and create a basis for developing temperature control strategies. The primary objective of the present study is to develop a modular dynamic TEG model applied to WHR for engines. In contrast to the previously mentioned dynamic TEG models [8,6,12,13,9], an important feature of the model is its ability to capture the dynamics of the temperatures for the hot end and outlet exhaust, which can be used for a model-based temperature control design. Another novelty of this paper is that more complete experimental validations are presented in this paper with experiments on both a TEM test rig and a TEG engine test bench.

2. Model development

2.1. Model structure

The configuration of a TEG system with counter flow type HXRs is presented in Fig. 1. The TEG system is symmetrical about the hot channel. For the purposes of analysis the structure of the TEG system, it is divided into three major regions: hot end, cold end, and central region. Both the hot and cold end are made up of a HXR and an aluminium plate. The hot side HXR can be connected to the exhaust line of an engine and cold side HXR is connected to an engine coolant or a separate chiller. The function of the aluminium plates is to even the temperature distribution along the flow direction and reduce the spreading resistance with their relatively higher thermal conductivity. Although aluminium plates contribute to an increase of thermal resistance, an optimal thickness of aluminium plate can increase the average delta temperature of all TEMs on the HXRs [16]. The central region consists of a number of TEMs and insulation materials. It is assumed that all the TEMs are evenly distributed on the surface of HXR and electrically connected in series. The air gap between the TEMs are filled with insulation materials, which can effectively reduce the possible heat leakage through the air gaps.

The TEG model can be divided into two models: a quasi-stationary TEM model and a dynamic TEG model. The quasi-stationary TEM model converts the thermal energy into electricity based on hot and cold side temperatures of the TEM. A quasi-stationary model is used because of the much faster electric response than thermal response [9]. Since the thermal masses of both sides of the HXRs are significantly larger than the TEMs and dominate the thermal dynamics of the TEG system, energy transfer at the hot and cold end of the TEG system are

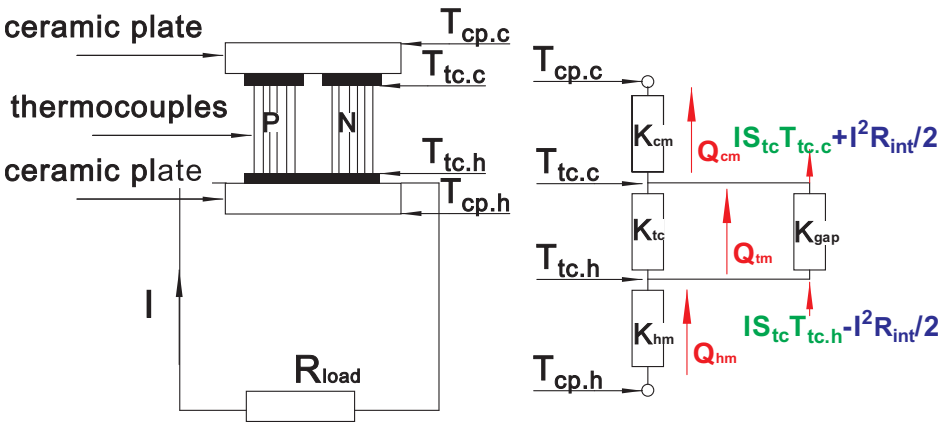

Fig. 3. Temperature distribution and energy balance in a TEM.

simulated by dynamic models. The structure and parameters of the model are shown in Fig. 2.

2.2. TEM model development

2.2.1. Assumption

The following assumptions are made for the TEM model

- Seebeck coefficient, thermal conductivity and electrical resistance of the material changes with the average temperature of the two sides of the thermocouple.
- The Thomson effect in the TEM can be neglected.
- Heat conduction through the conductive tabs is ignored.

2.2.2. TEM modelling

Most commercial TEMs are in planar forms, which can be seen in Fig. 3. A TEM mainly consists of thermocouple, ceramic plates and conductive tabs. A positive-type (p-type) thermoelectric element and a negative-type (n-type) one make up a thermocouple. The conductive tabs connect all the thermoelectric elements electrically in series and thermally in parallel between two ceramic plates. The ceramic plates are thermally conductive and electrically insulating. For a typical commercial TEM, both p-type and n-type thermoelectric elements are made in the same dimensions but different materials. The thermoelectric elements in most commercial modules are not closely arranged and air gap exists in the module.

The properties of the TEM can be calculated from material properties and geometrical parameters which can be easily obtained from the manufacturers' datasheet. The Seebeck coefficient S_{tc}, thermal conductance K_{tc} and electrical resistance R_{tc} of the thermocouples, thermal conductance of the air gap K_{gap} and ceramic plate K_{cp} are respectively calculated as follows:

$$S_{tc} = n_{tc}(S_p - S_n) \tag{1}$$

$$K_{tc} = \frac{n_{tc}A_{tc}(k_p + k_n)}{2l_{tc}} \tag{2}$$

$$R_{tc} = \frac{2n_{tc}l_{tc}}{A_{tc}}\left(\frac{1}{\sigma_p} + \frac{1}{\sigma_n}\right) \tag{3}$$

$$K_{gap} = \frac{k_{gap}(A_{cp} - n_{tc}A_{tc})}{l_{tc}} \tag{4}$$

$$K_{cp} = \frac{k_{cp}A_{cp}}{l_{cp}} \tag{5}$$

All these properties are temperature-dependent and here they are functions of an average temperature of the two sides of the thermocouple.

Fig. 3 depicts the temperature distribution in a TEM and its energy balance. $T_{cp.h}$, $T_{cp.c}$ and $T_{tc.h}$, $T_{tc.c}$ are respectively hot and cold side temperature of the ceramic plate and hot and cold side temperature of the thermocouples. Three effects are assumed to happen in the TEM and are presented in three different colours: Peltier effect (green[1]), Joule heating effect (blue), and Fourier effect (red). According to Fig. 3, the energy balance equations for the hot side and cold side of the thermocouples can respectively be expressed as [17]:

$$Q_{hm} = IS_{tc}T_{tc.h} + Q_{tm} - \frac{1}{2}I^2R_{int} \tag{6}$$

$$Q_{cm} = IS_{tc}T_{tc.c} + Q_{tm} + \frac{1}{2}I^2R_{int} \tag{7}$$

R_{int} is the overall electrical resistance of the TEM, which includes the electrical resistance of the thermocouples R_{tc} and electrical contact resistance R_{ct}.

$$R_{int} = R_{tc} + R_{ct} \tag{8}$$

Q_{hm} and Q_{cm} are respectively the heat conducted through the hot and cold side of the module. Q_{tm} includes the heat conducted though the thermocouples and the air gap between the thermocouples. They can be calculated respectively as follows:

$$Q_{hm} = K_{hm}(T_{cp.h} - T_{tc.h}) \tag{9}$$

$$Q_{cm} = K_{cm}(T_{tc.c} - T_{cp.c}) \tag{10}$$

$$Q_{tm} = (K_{tc} + K_{gap})(T_{tc.h} - T_{tc.c}) \tag{11}$$

where K_{hm} and K_{cm} are respectively the overall thermal conductance of hot and cold side of the module. They can be expressed as follows:

$$\frac{1}{K_{hm}} = \frac{1}{K_{cp}} + \frac{1}{K_{ct.h}} \tag{12}$$

$$\frac{1}{K_{cm}} = \frac{1}{K_{cp}} + \frac{1}{K_{ct.c}} \tag{13}$$

where $K_{ct.h}$ and $K_{ct.c}$ are respectively the hot and cold side thermal contact conductance, which include thermal contact conductance inside TEMs and between the TEMs and the aluminium plates.

Fig. 4 presents the electrical network of a TEM. Based on Seebeck effect, when there is temperature difference between a TEM, an open circuit voltage can be generated.

$$U_{TEM.ocv} = S_{tc}(T_{tc.h} - T_{tc.c}) \tag{14}$$

The current in the close-circuit can be expressed as:

$$I = \frac{U_{TEM.ocv}}{R_{int} + R_{load}} \tag{15}$$

The output voltage and power output of a TEM can be respectively expressed as:

$$U_{TEM.out} = U_{TEM.ocv} - IR_{int} \tag{16}$$

$$P_{TEM.out} = U_{TEM.out}I \tag{17}$$

2.2.3. TEM test rig setup

The performance of a TEM is evaluated using a test rig. The scheme of the test rig and its structure are shown in Fig. 5. The 300 mm^2 electric heating plate (3), which houses a 2.3 kW flexible heater element, is used as the heat source. The temperature of the heating plate is controlled by a heater control box (11). The heat sink is cooled by a circulated coolant (10). The TEM (6) is sandwiched by two aluminium plates (4, 5). The tested TEM is an European Thermodynamics module (GM250-127-28-10). Its properties can be found in Table 1. In the middle of each aluminium plate, there are holes (7, 8) to install thermocouple sensors to measure both hot and cold side temperatures of the TEM (T_{hd} and T_{cd}). Insulation materials (9) are used to fill the gap between the two aluminium plates and minimize the unwanted heat transfer. The bottle jack (1) makes sure the aluminium plates and TEM are in close contact by applying clamping force F, which can be measured by the load cell (2). An NI Crio-9024 DAQ chassis (12) and a computer (13) make up the data acquisition system, which records simultaneously the data from load cell (F), thermocouples sensor (T_{hd} and T_{cd}) and the output voltage of the TEM ($U_{TEM.out}$). The uncertainty for voltage and current measurements are respectively ±0.05 A and ±0.05 V.

2.2.4. Model tuning and validation

Due to the fabrication and connection method, R_{ct} and K_{ct} exist. Thus, the real tested properties of a TEM in the application can be different from a direct calculation from the materials and geometrical parameters [18,19]. R_{ct} mainly depends on contact pressure, properties

[1] For interpretation of color in 'Fig. 3', the reader is referred to the web version of this article.

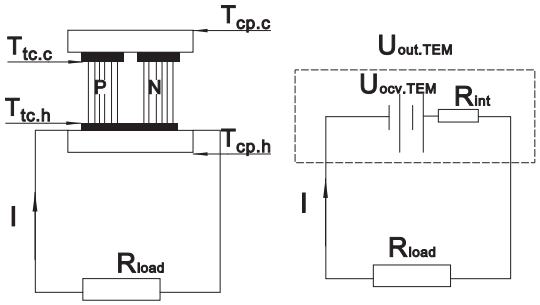

Fig. 4. Electrical network of a TEM.

temperature. Same aluminium plates and constant clamping force are used in each test. Thus, $K_{ct.h}$ and $K_{ct.c}$ are respectively expressed as the same linear functions of temperature, which are presented as follows:

$$K_{ct.h} = b_{ct.1} + b_{ct.2} T_{hd} \tag{19}$$

$$K_{ct.c} = b_{ct.1} + b_{ct.2} T_{cd} \tag{20}$$

$b_{ct.1}$ and $b_{ct.2}$ are tuning parameters.

Two experiments with different cold side temperatures T_{cd} are conducted here. Each experiment is repeated at least three times to obtain reproducible results. The mean value of the experimental data is used as the final experimental data. Before switching on the electric heating plate, the following operating conditions are set:

- The coolant temperature is set constant as T_{cd} = 30°C or 50°C.
- Using the bottle jack to set the clamping force F = 3000 N, which is about 0.8 MPa on the module.
- The electric load resistance R_{load} is set as 0.3Ω.

The experiment is started by switching on the electric heating plate

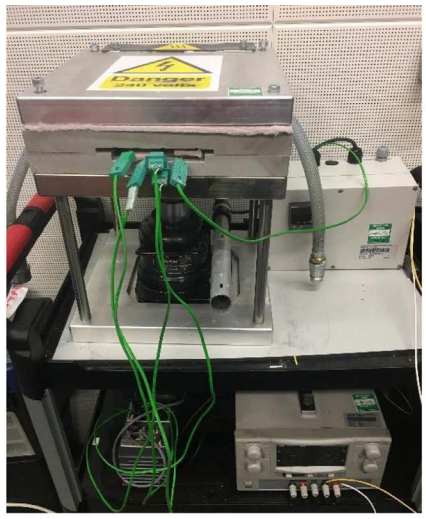

(a) TEM test rig.

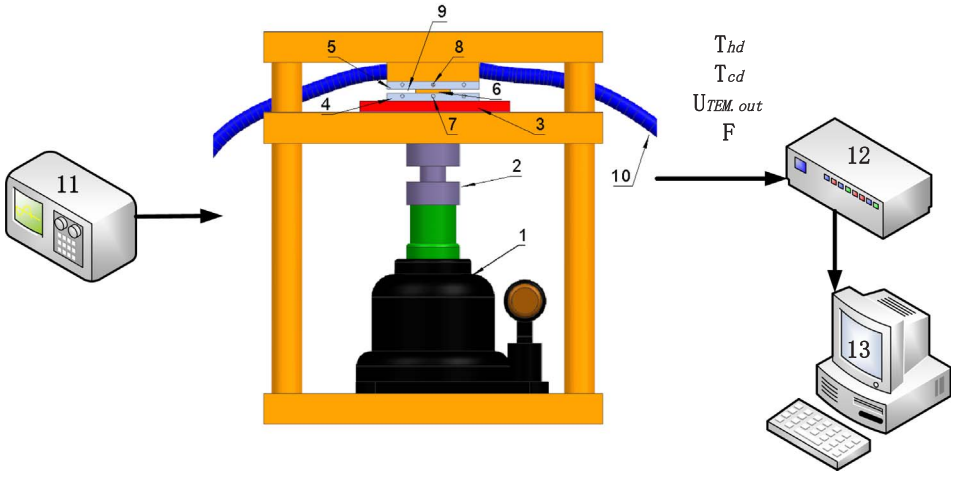

(b) test rig structured diagram.

Fig. 5. TEM test rig and its structure diagram.

of the contact materials and contact surface characteristics. Constant clamping force and same electrical connecting method are applied in all the tests. Thus, a constant R_{ct} is assumed in the TEM model.

$$R_{ct} = b_{ct.0} \tag{18}$$

$b_{ct.0}$ is the tuning parameter. The primary factors in determining the magnitude of K_{ct} are respectively contact pressure, properties of contact materials, contact surface characteristics, and the mean junction

Table 1
Datasheet of TEM GM250-127-28-10.

Area of a ceramic plate A_{cp}	$62 \times 62 \times 10^{-6}$ m^2
Area of a thermocouple A_{tc}	$2.8 \times 5.6 \times 10^{-6}$ m^2
Thickness of a thermocouple l_{tc}	1×10^{-3} m
Thickness of a ceramic plate l_{cp}	1.5×10^{-3} m
Thickness of a TEM l_{TEM}	4×10^{-3} m
Number of thermocouples n_{ct}	127
Thermal conductivity of the ceramic plate k_{cp}	35 W/(m K)
Thermal conductivity of the thermal elements	$k_p = (3.62T^2 - 2635T + 622162) \times 10^{-5}$ W/(m K)
	$k_n = (3.35T^2 - 2335T + 560633) \times 10^{-5}$ W/(m K)
Seebeck coefficient of the thermal elements	$S_p = (-3.63T^2 + 2743T - 296214) \times 10^3$ V/K
	$S_n = (1.53T^2 - 1080T - 28338) \times 10^3$ V/K
Electric conductivity of the thermal elements	$\sigma_p = 1.05T^2 - 1016T + 311371$ S/m
	$\sigma_n = 1.56T^2 - 1570T + 446638$ S/m
Max operation temperature	Hot side: 250 °C
	Cold side: 175 °C
Max compression	1 MPa

with a target temperature of 250°C. The hot side temperature T_{hd} begins to increase so does the output voltage $U_{TEM.out}$. T_{hd} and $U_{TEM.out}$ are simultaneously recorded by the data acquisition system.

The tuning parameters $b_{ct.0}$, $b_{ct.1}$, $b_{ct.2}$ are determined by solving a least-squares optimization problem that minimizes J_1, defined as:

$$J_1(b_{ct.0},b_{ct.1},b_{ct.2}) = (U_{TEM.out} - U_{TEM.out.meas})^2 \quad (21)$$

$U_{TEM.out}$ is the model output and $U_{TEM.out.meas}$ is measured data. Based on the experimental data, R_{ct}, $K_{ct.h}$ and $K_{ct.c}$ can be expressed respectively as follows:

$$R_{ct} = 0.11\ \Omega \quad (22)$$

$$K_{ct.h} = (-0.021 + 0.024T_{hd})\ \text{W/K} \quad (23)$$

$$K_{ct.c} = (-0.021 + 0.024T_{cd})\ \text{W/K} \quad (24)$$

Relative errors (error(i)) and mean absolute error (MAE) are calculated and used to evaluate the tuning and the validation of the model.

$$error(i) = \frac{y_{meas}(i) - y_{mod}(i)}{y_{meas}(i)} \times 100\% \quad (25)$$

$$MAE = \frac{\sum_{i=1}^{N} |error(i)|}{N} \quad (26)$$

where i and N are respectively an operating point and total number of operating points; y_{meas} and y_{mod} are respectively measured data and model output.

The comparison of the simulation results with the experimental data including error bars is presented in Fig. 6. It can be seen that both simulation results correspond well with the test results. The calculated MAE is about 2%. This validation shows that both the electrical contact resistance and thermal contact conductances give a good fit for the tested TEM.

2.3. TEG model development

2.3.1. Assumption

The following assumptions are made for the TEG model

- The main heat leakage is the heat flow through the insulation materials. Both radiative and convective heat loss from the TEG system to the surroundings are neglected.
- The flow rates for both exhaust gas and coolant are assumed to stay constant along the flow direction. Both exhaust gas and coolant density variation with temperature change in TEG are sufficiently small to have no practical effect on the predictions.
- Heat conduction along the flow rate direction is ignored in each control volume, as heat conduction perpendicular to the flow direction is dominant. Temperature inside each component is uniformly distributed in each control volume.
- The hot and cold ends of the TEG are assumed to be lumped-capacity systems.

2.3.2. TEG modelling

The TEG model is discretized into small control volumes along the length of TEG. In this way, the variation of fluid properties and TEM's performance changing with temperature along the flow direction are taken into consideration. Since the TEG is symmetric with respect to its height, only half of the domain is simulated here. As shown in Fig. 7 the TEG is equally divided into n_{CV} control volumes. The heat transfer area, mass of the HXRs and aluminium plate for each control volume can be expressed as follow:

$$A_{hxr.CV} = \frac{A_{hxr}}{n_{CV}} \quad (27)$$

$$A_{cxr.CV} = \frac{A_{cxr}}{n_{CV}} \quad (28)$$

$$A_{Ins.CV} = \frac{A_{Ins}}{n_{CV}} \quad (29)$$

$$M_{hxr.CV} = \frac{M_{hxr}}{2n_{CV}} \quad (30)$$

$$M_{cxr.CV} = \frac{M_{cxr}}{n_{CV}} \quad (31)$$

$$M_{ap.CV} = \frac{M_{ap}}{n_{CV}} \quad (32)$$

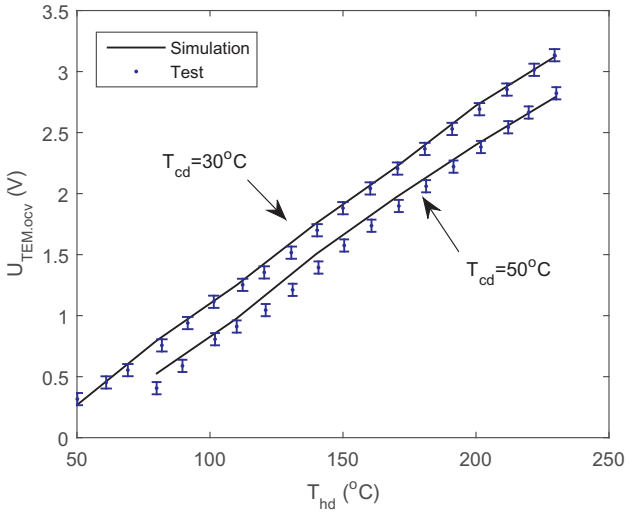

Fig. 6. Experimental data and simulation results of TEM test with error bars.

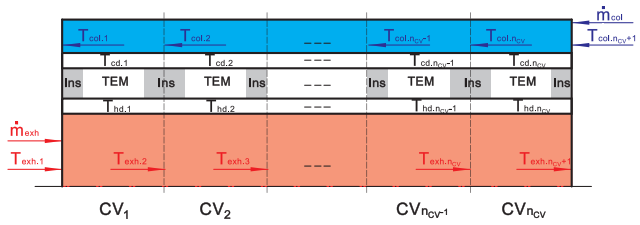

Fig. 7. Space discretization of the TEG.

Each control volume has its own inlet and outlet exhaust temperature and coolant temperature. The outlet temperatures of a control volume are also the inlet temperatures for the control volume next to it. In each control volume, it is assumed that there is a uniform distribution of TEMs: one TEM in flow direction and n_{TEM} TEMs in perpendicular to the flow direction.

Since all the control volumes have the same structure, here the *i*th control volume is chosen as an example. The temperature distribution and energy transfer in the *i*th control volume are presented in Fig. 8. $T_{exh.i}$, $T_{exh.i+1}$, $T_{col.i+1}$, $T_{col.i}$ are respectively exhaust gas-in temperature, exhaust gas-out temperature, coolant-in temperature, and coolant-out temperature. $T_{hd.i}$ and $T_{cd.i}$ are respectively the temperature for the hot and cold end. The temperature drop or increase of the fluid in both sides of the heat exchangers can be modelled by solving a simple partial differential equation [20]. The gas-out temperature $T_{exh.i+1}$ and coolant-out temperature $T_{col.i}$ can be respectively expressed as:

$$T_{exh.i+1} = T_{hd.i} + (T_{exh.i} - T_{hd.i}) e^{-\frac{h_{hxr} A_{hxr.CV}}{c_{exh} \dot{m}_{exh}}} \tag{33}$$

$$T_{col.i} = T_{cd.i} - (T_{cd.i} - T_{col.i+1}) e^{-\frac{h_{cxr} A_{cxr.CV}}{c_{col} \dot{m}_{col}}} \tag{34}$$

where h_{hxr} and h_{cxr} are respectively the heat transfer coefficient of the hot and cold side HXR.

By treating both hot and cold ends as lumped-capacity systems and assuming infinitely fast conductivity along the flow direction, the energy equations for hot end and cold end are expressed respectively as:

$$(M_{hxr.CV} c_{hxr} + M_{ap.CV} c_{ap}) \frac{dT_{hd.i}}{dt} = Q_{hxr.i} - Q_{hm.i} - Q_{Ins.i} \tag{35}$$

$$(M_{cxr.CV} c_{cxr} + M_{ap.CV} c_{ap}) \frac{dT_{cd.i}}{dt} = Q_{Ins.i} + Q_{cm.i} - Q_{cxr.i} \tag{36}$$

$Q_{hm.i}$ and $Q_{cm.i}$ are respectively the heat conducted from the hot end to the central section and the heat conducted from the central section to the cold end. Based on energy conservation and the symmetrical characteristics of the TEG system, the heat absorbed by the hot side HXR $Q_{hxr.i}$ and the heat dissipated to cold side HXR $Q_{cxr.i}$ can respectively be expressed as follows:

$$Q_{hxr.i} = \frac{1}{2} (T_{exh.i} - T_{exh.i+1}) \dot{m}_{exh} c_{exh} \tag{37}$$

$$Q_{cxr.i} = (T_{col.i} - T_{col.i+1}) \dot{m}_{col} c_{col} \tag{38}$$

$Q_{Ins.i}$ is the heat conducted through the insulation materials between the TEMs, which can be expressed as:

$$Q_{Ins.i} = K_{Ins} (T_{hd.i} - T_{cd.i}) \tag{39}$$

where K_{Ins} is the thermal conductance of the insulation materials, which can be calculated by:

$$K_{Ins} = \frac{k_{Ins} A_{Ins.CV}}{l_{TEM}} \tag{40}$$

Since the hot end and cold end are closely connected to the hot sides and cold sides of the TEMs, the hot end and cold end temperatures $T_{hd.i}$ and $T_{cd.i}$ are assumed respectively to be equal to the previous hot side and cold side temperatures of the TEM $T_{cp.h}$ and $T_{cp.c}$.

$$T_{hd.i} = T_{cp.h} \tag{41}$$

$$T_{cd.i} = T_{cp.c} \tag{42}$$

It is assumed that $T_{hd.i}$ and $T_{cd.i}$ are distributed uniformly in each control volume. $Q_{hm.i}$ and $Q_{cm.i}$, which can then be calculated based on the previous TEM model, are expressed respectively as follows:

$$Q_{hm.i} = n_{TEM} Q_{hm} \tag{43}$$

$$Q_{cm.i} = n_{TEM} Q_{cm} \tag{44}$$

Then, the hot and cold side temperatures of the TEM $T_{cp.h}$ and $T_{cp.c}$ can be solved. Based on the previous TEM model, both the output voltage of the TEM $U_{TEM.out}$ and its power output $P_{TEM.out}$ can be calculated. Since all the TEMs are connected in series and the TEG system is symmetrical, the overall output voltage $U_{CVi.out}$ and power output $P_{CVi.out}$ in *ith* CV can be expressed respectively as follows:

$$U_{CVi.out} = 2 n_{TEM} U_{TEM.out} \tag{45}$$

$$P_{CVi.out} = 2 n_{TEM} P_{TEM.out} \tag{46}$$

The overall output voltage $U_{out.TEG}$ and power output $P_{TEG.out}$ of the TEG system can be expressed respectively as:

$$U_{TEG.out} = \sum_{i=1}^{n_{CV}} U_{CVi.out} \tag{47}$$

$$P_{TEG.out} = \sum_{i=1}^{n_{CV}} P_{CVi.out} \tag{48}$$

2.3.3. TEG engine test bench setup

The scheme of the TEG engine test bench and its structure are shown in Fig. 9. The engine used in this study is a CAT C6.6 heavy-duty diesel engine. This is a six cylinder, 6.6 l engine equipped with a common rail fuel system. This engine is installed in a test bed with a Froude AG400-HS eddy current dynamometer controlled by a CP Engineering Cadet V14 dynamometer control system. The TEG system is mounted on the exhaust gas recirculation (EGR) path of the engine, which has been specially modified for the purposes of the TEG research. The EGR valve is used to control the flow rate and protect the TEG system in high temperatures. Four European Thermodynamics modules (GM250-127-28-10) are sandwiched assembled with two TEMs on each side of the hot side HXR. All the TEMs are electrically connected in series with

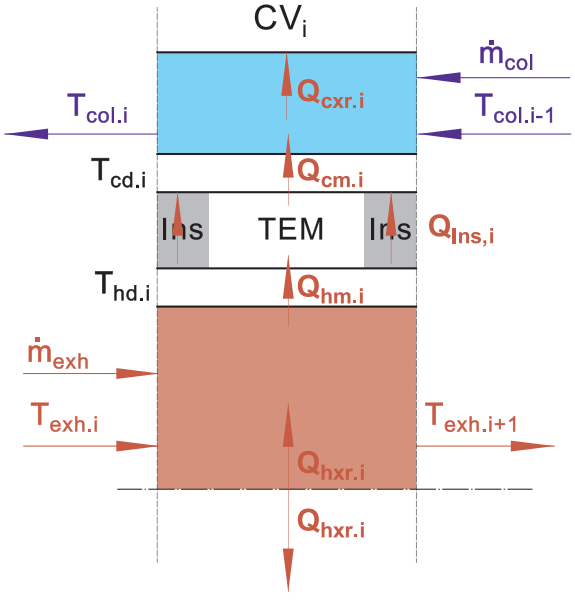

Fig. 8. Temperature distribution and energy transfer in *i*th control volume.

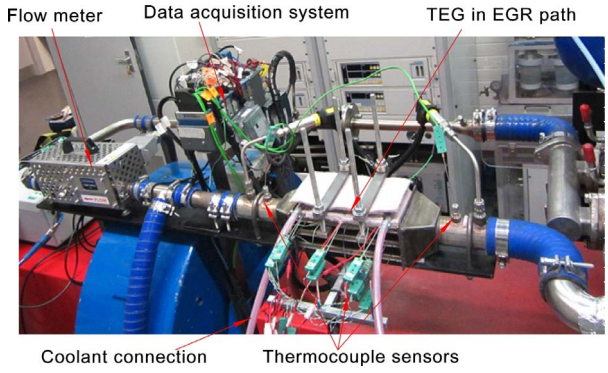

(a) TEG engine test bench.

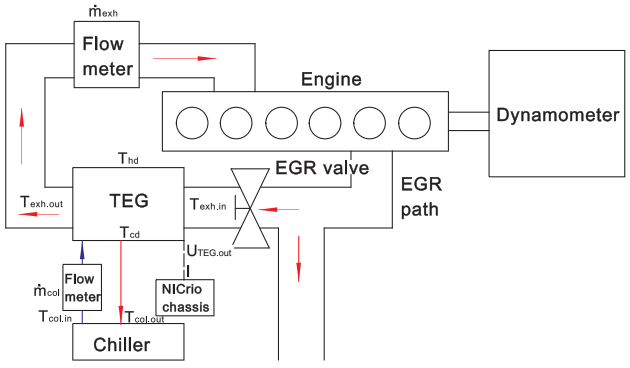

(b) TEG engine test bench structured diagram.

Fig. 9. The TEG engine test bench and its structure diagram.

Table 2
Datasheet of the TEG used in EGR path.

Number of control volumes n_{CV}	2
Number of TEMs in a control volume n_{TEM}	1
Heat transfer area of the hot side HXR A_{hxr}	0.16 m^2
Heat transfer area of the cold side HXR A_{cxr}	0.024 m^2
Area of the overall insulation materials on one side A_{Ins}	0.017 m^2
Hydraulic diameter of hot side HXR D_{hxr}	0.013 m
Hydraulic diameter of cold side HXR D_{cxr}	0.007 m
Mass of the hot side HXR M_{hxr}	0.64 kg
Mass of the cold side HXR M_{cxr}	3 kg
Mass of an aluminium plate M_{ap}	0.05 kg
Specific heat capacity of the hot side HXR c_{hxr}	500 J/(kg K))
Specific heat capacity of the cold HXR c_{cxr}	950 J/(kg K))
Specific heat capacity of the aluminium plate c_{ap}	900 J/(kg K))
Thermal conductivity of insulation materials k_{Ins}	0.025 W/(m K)

R_{load}. The same clamping force (F = 3000 N) is applied, which is measured by a load cell. The parameters of the TEG system are presented in Table 2. The cold side of the TEG is maintained using chilled water from a laboratory recirculation chiller. The temperatures are measured by a number of thermocouple sensors, which are respectively installed upstream and downstream of the hot side HXR ($T_{exh.in}$ and $T_{exh.out}$), upstream and downstream of the cold side HXR ($T_{col.in}$ and $T_{col.out}$), and in the hot and cold side aluminium plates (T_{hd} and T_{cd}). Flow meters are used to measure the flow rates of exhaust gas in the EGR path $\dot{m}_{exh}$ and coolant $\dot{m}_{col}$. The data acquisition system used in the experimental work consists of a NI CRIO chassis and a 16bit analog input module. It simultaneously records the data of all the temperatures and voltage $U_{TEG.out}$ and current I. The uncertainty for voltage and current measurements are respectively ±0.05 A and ±0.05 V. The maximum uncertainty for measuring the temperature is ±1°C. Then according to the

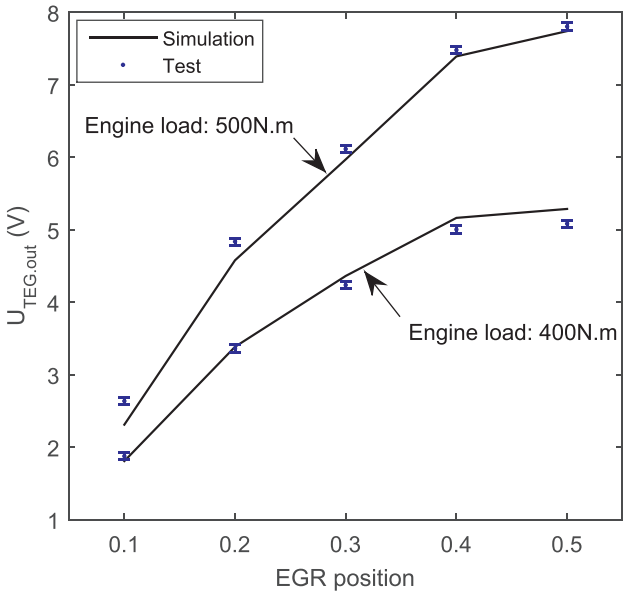

(a) Output voltage at different EGR positions with error bars

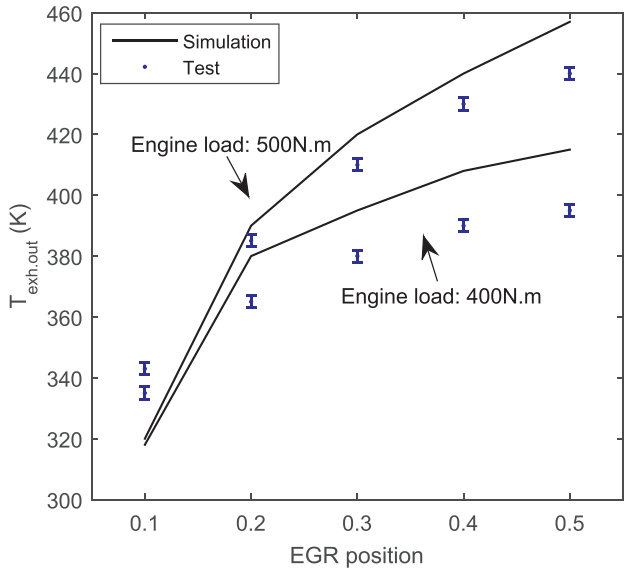

(b) Gas-out temperature at different EGR positions with error bars

Fig. 10. Experimental data and simulation results at different EGR positions.

uncertainty analysis theory, the maximum uncertainty of the computed electrical power is about ±5%.

2.3.4. Model tuning and validation

A majority of Refs. [6,9,8,13,21] point out the heat transfer coefficient of the HXR in the form of Nusselt-Reynolds-Prandtl relations. However, there is a large variations in the expression of Nusselt numbers due to its high variability in the exhaust heat transfer [22]. Thus, the heat transfer coefficient of HXR needs to be tuned based on the tested HXR. The heat transfer coefficients of hot and cold side HXRs h_{hxr} and h_{cxr} can be expressed as Nusselt-Reynolds-Prandtl relations as follows:

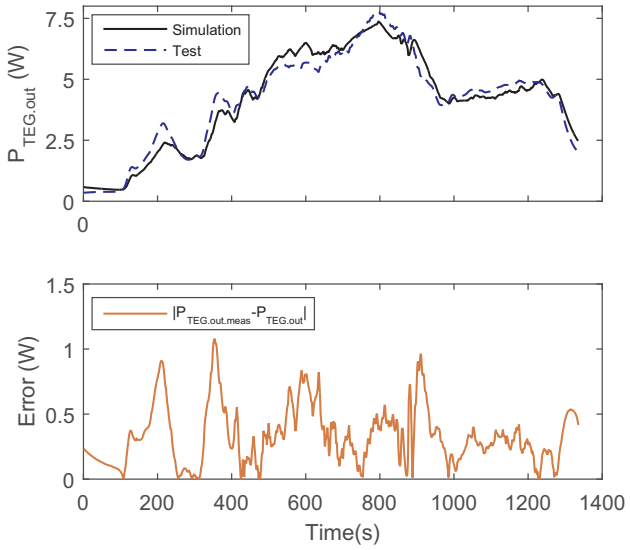

Fig. 11. Experimental data and simulation results of NRTC for $P_{TEG.out}$.

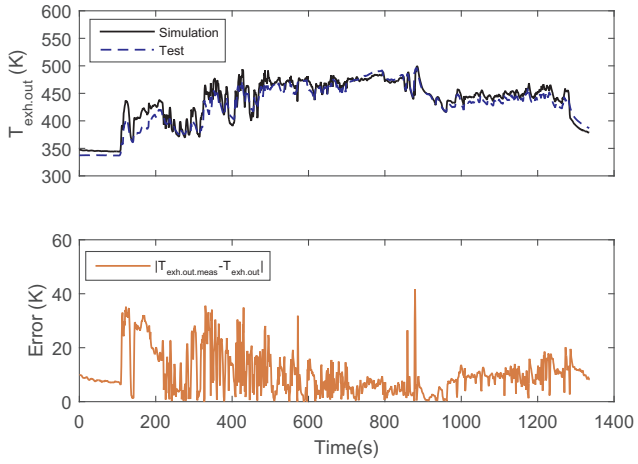

Fig. 12. Experimental data and simulation results of NRTC for $T_{exh.out}$.

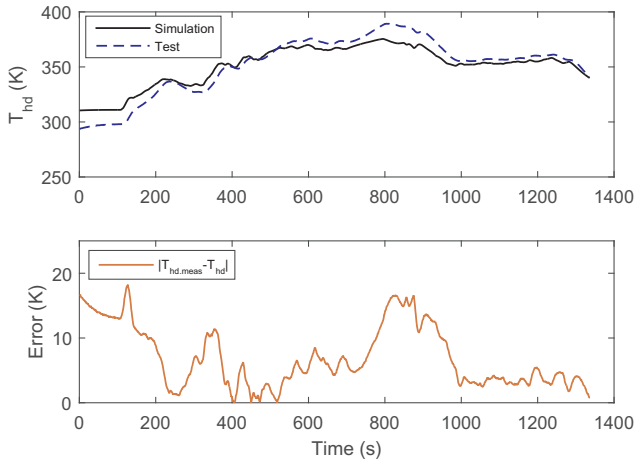

Fig. 13. Experimental data and simulation results of NRTC for T_{hd}.

$$h_{hxr} = \frac{Nu}{D_{hxr}} k_{exh} = \frac{b_{hxr.0} Re^{b_{hxr.1}} Pr^{b_{hxr.2}}}{D_{hxr}} k_{exh} \tag{49}$$

$$h_{cxr} = \frac{Nu}{D_{cxr}} k_{col} = \frac{b_{cxr.0} Re^{b_{cxr.1}} Pr^{b_{cxr.2}}}{D_{cxr}} k_{col} \tag{50}$$

where D_{hxr} and D_{cxr} are respectively the hydraulic diameters for hot and cold side HXRs. The tuning parameters for the TEG model are $b_{hxr.0}$, $b_{hxr.1}$, $b_{hxr.2}$ for h_{hxr} and $b_{cxr.0}$, $b_{cxr.1}$, $b_{cxr.2}$ for h_{cxr}.

The tuning and validation of the TEG model is based on a validated TEM model and is conducted in two steps. First of all, measurements of the TEG performance at steady-state engine operating points are used to tune the heat transfer coefficients of both side HXRs. Secondly, measurements of the TEG performance at transient engine cycle test are used to compared with the model output and validate the model.

Ten steady-state TEG engine tests with five different EGR positions and two different engine loads are conducted here. Test data is recorded when it is stable. Each test is repeated at least three times to obtain reproducible results. The mean value of the experimental data is used as the final experimental data. The steady-state data is measured under the specific operating conditions as follows:

- Engine speed is set as constant 1500 rpm.
- R_{load} is set as constant 10Ω.
- Coolant temperature and flow rate are set respectively as 10°C and 0.095 kg/s.
- Engine load is set as constant 400 N m or 500 N m.
- The EGR value positions are set as 0.1, 0.2, 0.3, 0.4 and 0.5 respectively.

Since the same clamping force, TEMs, aluminium plates, and electrical connecting method are used, the tuning parameters of the TEM model are assumed to be the same for the TEG model validation. Based on the steady-state date from TEG engine test, the tuning parameters for the TEG model are estimated using a least-squares optimization that minimizes errors both in output voltage and exhaust gas-out temperature.

$$\begin{aligned} &min\ J_2(b_{hxr.0},b_{hxr.1},b_{hxr.2},b_{cxr.0},b_{cxr.1},b_{cxr.2}) \\ &b_{hxr.0},b_{hxr.1},b_{hxr.2},b_{cxr.0},b_{cxr.1},b_{cxr.2} \\ &\subseteq \text{ feasible set of heat transfer coefficients} \end{aligned} \tag{51}$$

where J_2 is the cost function given by

$$J_2 = (U_{TEG.out} - U_{TEG.out.meas})^2 + (T_{exh.out} - T_{exh,out.meas})^2 \tag{52}$$

$U_{TEG.out}$ and $T_{exh.out}$ are respectively model output and $U_{TEG.out.meas}$ and $T_{exh.out.meas}$ are respectively measured data.

The final tuning results for h_{hxr} and h_{cxr} are expressed as follows:

$$h_{hxr} = \frac{0.99 Re^{0.0002} Pr^{0.33}}{D_{hxr}} k_{exh} \tag{53}$$

$$h_{cxr} = \frac{0.023 Re^{0.8} Pr^{0.33}}{D_{cxr}} k_{col} \tag{54}$$

A comparison of the simulation and test results including error bars for $U_{TEG.out}$ and $T_{exh.out}$ at different EGR positions is plotted in Fig. 10. It can be seen that both simulation results correspond well with the test results. The calculated MAE for $U_{TEG.out}$ and $T_{exh,out}$ are 3.8% and 4.6% respectively. The relatively bigger errors for $T_{exh,out}$ can be explained as follows. The underestimation of $T_{exh,out}$ at lower EGR values is due to the measurements of $T_{exh,out}$ being influenced by the relatively higher temperature of the pipe wall when $\dot{m}_{exh}$ is low. The overestimation at higher EGR values can be explained by neglecting the effects of radiation and convection to the ambient when developing the TEG model.

A non-road transient cycle (NRTC) is conducted in the TEG engine test bench to validate the TEG model. NRTC is the type test cycle specified for non-road applications of heavy duty engines to be sold in the USA and the EU The NRTC is specified by the EPA [23]. In order to limit the maximum temeprature seen by the TEMs to 250°C, the NRTC torque profile was scaled to 0.3 of its normal value. The dynamic data is measured under the specific operating conditions as follows:

- Engine is set to run 30% torque NRTC.

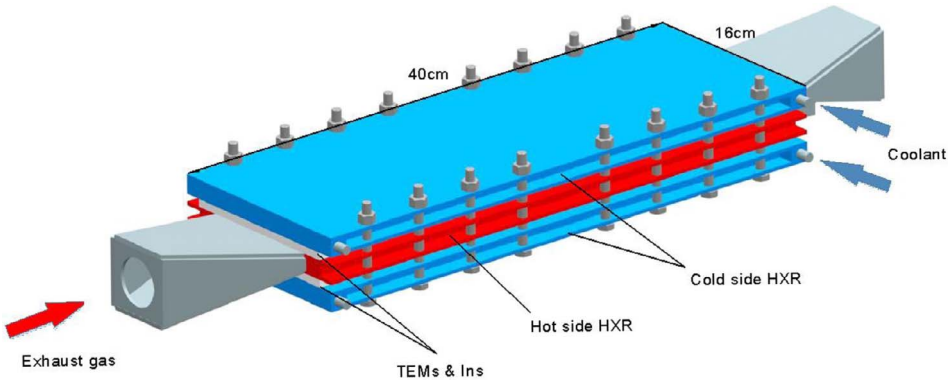

Fig. 14. The simulated TEG system used for WHR in a diesel engine.

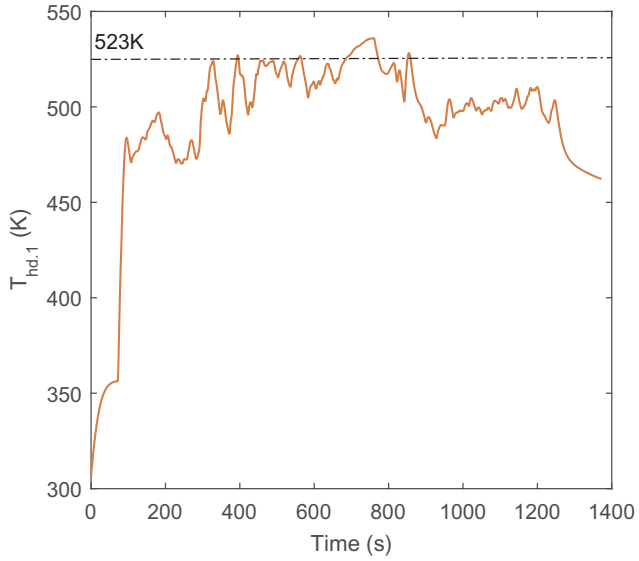

Fig. 15. The simulated hot end temperature.

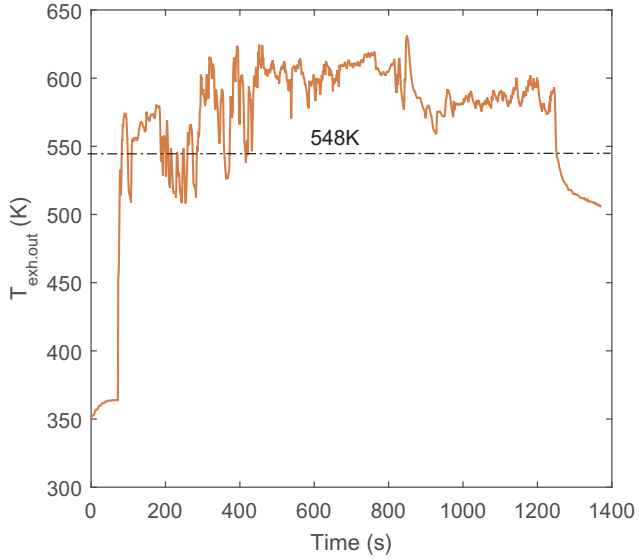

Fig. 16. The simulated outlet temperature.

- Coolant temperature and flow rate are set respectively as 10°C and 0.095 kg/s.
- The EGR value positions is set as 0.5.
- R_{load} is set as constant 0.3Ω.

The comparison between the simulation results and test date for $P_{TEG.out}$ of NRTC is presented in Fig. 11. It shows a good agreement between the simulation and experimental results. The mean difference between measurement and simulation is 0.33 W, which is 7% regarding average power output of the cycle. The maximum deviation is around 1 W, which occur at operating points of sudden torque change. This can be explained by the uncertainty in heat transfer coefficients and inertia of the test equipment.

Figs. 12 and 13 respectively show comparisons of predicted and measured gas-out temperature ($T_{exh.out} = T_{exh.3}$) and hot end temperature ($T_{hd} = \frac{T_{hd.1}+T_{hd.2}}{2}$). The simulation result shows that the dynamics of both $T_{exh.out}$ and T_{hd} are well captured by the model. In comparison with the measured data, the average absolute error for $T_{exh.out}$ is 10 K and the maximum deviation is 41 K, which happens at time periods with intensive temperature fluctuation caused by sudden torque change. For T_{hd}, the average absolute error is 7 K and the maximum error is about 18 K, which occur at the beginning of the test cycle and also at the temperature fluctuation period. The error at the beginning is due to the start up process of the model itself.

$T_{exh.out}$ and T_{hd} are both crucial for the control of the TEG system. When a TEG is installed upstream of an after-treatment system, $T_{exh.out}$ directly influences its performance. To minimize the influence on the after-treatment system, a control system is needed to maintain $T_{exh.out}$ to the normal operating temperature range of the after-treatment system. For a wide fluctuation of exhaust temperatures, the possible damage for the TEG system mainly comes from overheating of the hot side of the TEMs. However, higher hot side temperature gives higher power output of TEMs. Thus, a control system is needed to maintain high T_{hd} but below the maximum of the TEM's operating range. It can be seen from Figs. 12 and 13 that the model effectively captures the dynamics of $T_{exh.out}$ and T_{hd}. It can be concluded that the TEG dynamic model is able to be used as the basis for model-based temperature control design.

3. Results and discussion

This dynamic model serves two major purposes: performance prediction and as a basis for developing temperature control strategies. These two applications are presented in the following sections.

To fully present these two application, the validated TEG model is integrated with other exhaust system components in the model of a heavy duty engine with the TEG model located upstream of the after-treatment system. It is assumed that the cold side of the TEG is supplied with coolant at the normal operating temperature of the engine. The TEG, shown in Fig. 14, is assumed to be 16 cm wide by 40 cm long, with 10 ($n_{CV} = 5$, $n_{TEM} = 2$) TEMs (GM250-127-28-10) on each side. All the 20 TEMs are electrically connected in series with $R_{load} = 6\Omega$, which is matched to the internal resistance of the TEG system. The exhaust conditions upstream of the after-treatment system during an NRTC run on the test engine are used as inputs to the model. Coolant conditions are assumed constant with a temperature of 80°C and flow rate of

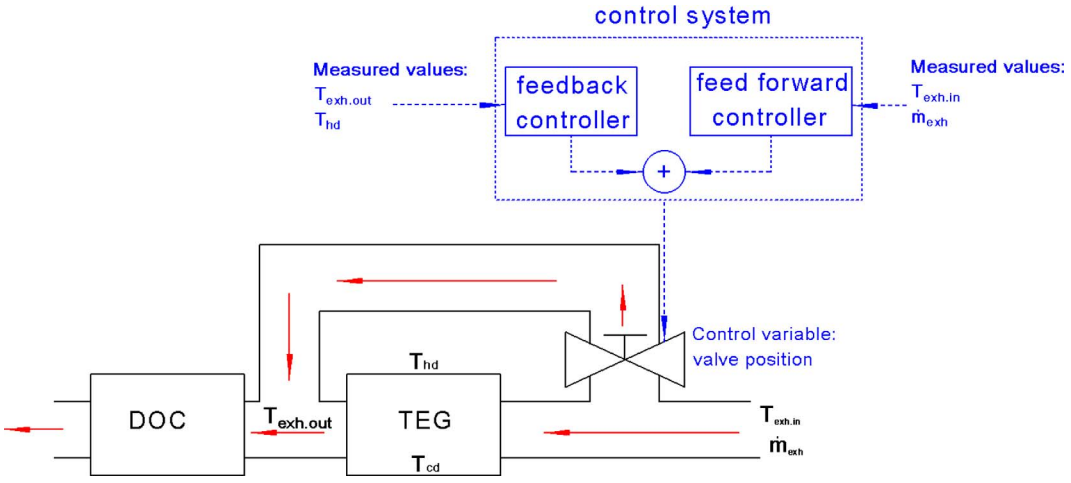

Fig. 17. A bypass control system of the TEG system.

Table 3
Definition of two prediction scenarios.

Parameters	Scenario 1	Scenario 2
h_{hxr}	105–125 W/m^2 K	130–150 W/m^2 K
h_{cxr}	3784 W/m^2 K	4730 W/m^2 K
R_{ct}	0.1 Ω	0.08 Ω
K_{ct}	10–13 W/K	12–15.6 W/K

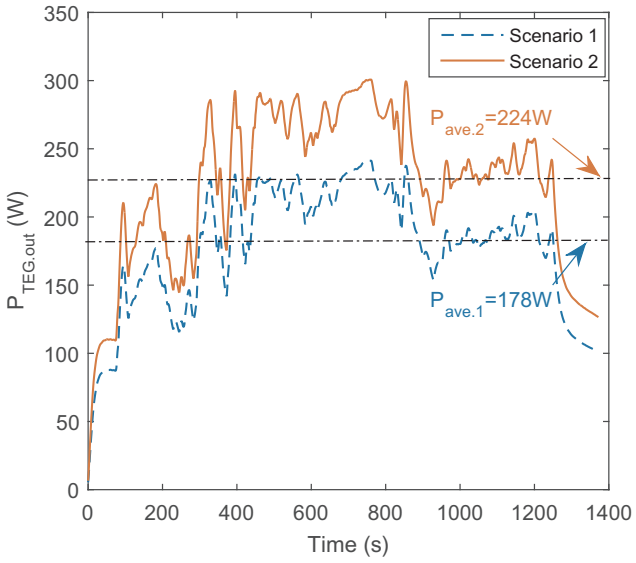

Fig. 18. The simulated power output.

0.2 kg/s.

3.1. Hot end and outlet temperature prediction

The evolution of the hot end temperature in the first control volume is depicted in Fig. 15. $T_{hd.1}$ shows a response with a time constant of about 50 s. The results indicate that there exists a hysteresis in the response of $T_{exh.in}$ to $T_{hd.1}$. The hysteresis is attributed to the delay of thermal diffusion from the exhaust gas to the ceramic plate. For most of the time, $T_{hd.1}$ is below the maximum temperature limit (523 K) of the TEMs. While in the time 394 s, 560 s, 689 s, 852 s, $T_{hd.1}$ exceeds 523 K, which threatens the integrity of the TEMs. In order to protect the TEMs, a temperature control is needed to lower the hot end temperature so as to ensure that the maximum temperature limit is not exceeded.

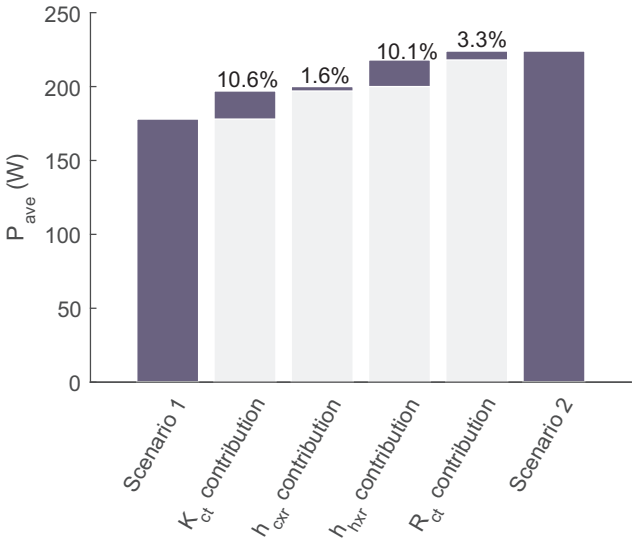

Fig. 19. Contribution of parameters to the improvement of power.

Fig. 16 shows the outlet temperature from the TEG. The Diesel Oxidation Catalyst-Diesel Particulate Filter (DOC-DPF) system applied for after-treatment in non-road diesel engines requires an exhaust temperature management mode to ensure inlet exhaust temperatures above the DOC light-off temperature (548 K) [24]. Here 548 K is used as a criterion for $T_{exh.out}$ to ensure an effective operation of the after-treatment system. Most of time in NRTC, $T_{exh.out}$ is above the temperature criterion of after-treatment system. Only at the time 100 s, 200 s, 300 s, 400 s, 480 s, 1280 s, a temperature control strategy needs to be adopted to maintain the outlet temperature of the TEG.

To control the temperature so as to ensure safety operation of the TEG and effective operation of the after-treatment system, a bypass solution is proposed here. It is shown in Fig. 17 that a bypass exhaust gas circuit is designed in the TEG system. When the bypass valve is open, the exhaust heat is shunted to the DOC. Protecting the TEG and maintain the minimum temperature of the DOC can both be achieved by adjusting the bypass value position. Both a feedback controller and a feed forward controller act on the bypass value position. The feedback controller establishes a feedback loop based on the measured temperatures of T_{hd} and $T_{exh.out}$. To react adequately to the sudden changes in exhaust path, an additional feed forward controller is implemented. Based on the measured $T_{exh.in}$ and $\dot{m}_{exh}$, a prediction for T_{hd} and $T_{exh,out}$ is made by the dynamic TEG model (see Fig. 17).

3.2. TEG power output prediction

For practical applications, the TEG systems not only need development of the better-performing TEMs and the high-efficient HXRs but also development of the integrated system. The thermal contact conductance K_{ct} and electrical contact resistance R_{ct} always exist at the interfaces between different materials. These thermal and electrical resistance cause loss of the overall output power of the TEG system. In order to investigate the influences of h_{hxr}, h_{cxr}, R_{ct} and K_{ct} on the power output of the TEG, two scenarios with different tuning parameters are presented. Their parameters are listed in Table 3. h_{hxr}, h_{cxr}, R_{ct} and K_{ct} in scenario 1 are using the same functions of the validated model. Compared with the scenario 1, some changes are made for the scenario 2: h_{hxr}, h_{cxr}, K_{ct} are both 20% higher than the scenario 1 but R_{ct} is 20% lower.

Fig. 18 shows the evolution of electric power output $P_{TEG.out}$ in both scenarios together with average values. It can be seen that both TEGs work effectively and show a quick response, and reach their average power output within 200s. The average power output in the second scenario is 224 W, which is 25.8% more than the first scenario (178 W). The maximum $P_{TEG.out}$ in the second scenario reaches is 300 W.

$P_{TEG.out}$ in the scenario 2 is always higher than the scenario 1 due to the parameters of h_{hxr}, h_{cxr} R_{ct} and K_{ct}. Their contributions to the improvement of power output are analysed by comparing average power outputs. Fig. 19 presents the improvements of power outputs with the change of parameters K_{ct}, h_{cxr}, h_{hxr} and R_{ct} respectively from the scenario 1 to the scenario 2. As can be seen that the biggest contribution to the improvement of electric power comes from the improvement of K_{ct}, which brings 10.6% average power increase. The second biggest contribution is h_{hxr} with 10.1% average power increase. In comparison, h_{cxr} and R_{ct} have relatively lower influence on the electric power output with respectively 1.6% and 3.3% improvements. As a conclusion, the integration of TEMs with the HXRs and the design of hot side HXR are of importance for the overall power outputs. K_{ct} is primarily a function of the pressure on the interface, contact materials, contact surface characteristics. Thus, increasing clamping force, using better thermal interface materials and better methods of integrating the TEMs onto the HXR surface are effective approaches. For the design of hot side HXR, a structural optimization to increase the turbulence intensity of the exhaust gas is suggested.

4. Conclusions

A dynamic TEG model for vehicle applications is developed and presented in this paper. By building models from thermoelectric materials into a TEM model, the high temperature dependence of material properties is considered. Based on a control volume approach, the gas properties and heat transfer along the HXR is more precisely described. Thermal inertia of the HXRs is taken into account in the model so that dynamic behaviour of the system is included. Steady-state measurement is carried out in TEM test rig and both steady-state and transient measurements are performed on a diesel engine equipped with a TEG in the EGR path. Based on these test data, the least-squares optimization strategy is used for model tuning. These makes the model tuning and validation process in this paper is more complete than the previous papers. Simulation results show that the dynamic TEG model can predict its dynamics with good accuracy. The maximum deviation for the power output and the temperatures are respectively 1 W and 41 K.

The power output for a TEG located upstream of an after-treatment system has been accurately predicted for the duration of a transient test cycle. The simulation results of power outputs show a TEG with 20 TEMs can produce average 170–224 W electric power. The model also successfully predicts the hot end temperature and outlet gas temperature of the TEG. This aspect of the model indicates its utility in the design of a control system to protect the TEMs and to ensure effective operation of the after-treatment system.

By analysing the parameters' effects, it was found out that K_{ct} and h_{hxr} have major influences on the overall power produced. Optimized K_{ct}, h_{cxr}, h_{hxr}, and R_{ct} can achieve 25.8% overall power output improvement. The results can be used as a guidance for optimization design of a TEG system. Future work will focus on optimizing integration of TEMs on the HXRs and configuration of the hot side HXR.

Acknowledgements

The authors would like to gratefully acknowledge the UK Engineering and Physical Sciences Research Council (EPSRC) for funding this research work under Grant No. EP/K026658/1. The authors would also like to thank Graham Smith, Iain Harber, Dominic Mckean and Steve Horner from Powertrain Lab in Loughborough University for their support to the engine experimental setup and throughout the engine testing.

References

[1] He W, Zhang G, Zhang X, Ji J, Li G, Zhao X. Recent development and application of thermoelectric generator and cooler. Appl Energy 2015;143:1–25.
[2] Aghaali H, Ångström H-E. A review of turbocompounding as a waste heat recovery system for internal combustion engines. Renew Sustain Energy Rev 2015;49:813–24.
[3] Wang T, Luan W, Wang W, Tu S-T. Waste heat recovery through plate heat exchanger based thermoelectric generator system. Appl Energy 2014;136:860–5.
[4] Yang Z, PradoGonjal J, Phillips M, Lan S, Powell A, Vaqueiro P et al. Improved thermoelectric generator performance using high temperature thermoelectric materials. Tech rep. SAE Technical Paper; 2017.
[5] Liang G, Zhou J, Huang X. Analytical model of parallel thermoelectric generator. Appl Energy 2011;88(12):5193–9.
[6] Gou X, Yang S, Xiao H, Ou Q. A dynamic model for thermoelectric generator applied in waste heat recovery. Energy 2013;52:201–9.
[7] Liu X, Li C, Deng Y, Su C. An energy-harvesting system using thermoelectric power generation for automotive application. Int J Electr Power Energy Syst 2015;67:510–6.
[8] Yu S, Du Q, Diao H, Shu G, Jiao K. Start-up modes of thermoelectric generator based on vehicle exhaust waste heat recovery. Appl Energy 2015;138:276–90.
[9] Meng J-H, Zhang X-X, Wang X-D. Dynamic response characteristics of thermoelectric generator predicted by a three-dimensional heat-electricity coupled model. J Power Sources 2014;245:262–9.
[10] Gou X, Xiao H, Yang S. Modeling, experimental study and optimization on low-temperature waste heat thermoelectric generator system. Appl Energy 2010;87(10):3131–6.
[11] Liang X, Sun X, Tian H, Shu G, Wang Y, Wang X. Comparison and parameter optimization of a two-stage thermoelectric generator using high temperature exhaust of internal combustion engine. Appl Energy 2014;130:190–9.
[12] Meng F, Chen L, Sun F. Effects of temperature dependence of thermoelectric properties on the power and efficiency of a multielement thermoelectric generator. Int J Energy Environ 2012;3(1):137–50.
[13] He W, Wang S, Yue L. High net power output analysis with changes in exhaust temperature in a thermoelectric generator system. Appl Energy 2017;196:259–67.
[14] Hsu C-T, Huang G-Y, Chu H-S, Yu B, Yao D-J. An effective Seebeck coefficient obtained by experimental results of a thermoelectric generator module. Appl Energy 2011;88(12):5173–9.
[15] Rosenberger M, Dellner M, Kluge M, Tarantik KR. Vehicle integration of a thermoelectric generator. MTZ Worldwide 2016;77(4):36–43.
[16] Yang Z, Lan S, Stobart R, Winward E, Chen R, Harber I. A comparison of four modelling techniques for thermoelectric generator. Tech rep. SAE Technical Paper; 2017.
[17] Rowe DM. CRC handbook of thermoelectrics. CRC Press; 1995.
[18] Bjørk R. The universal influence of contact resistance on the efficiency of a thermoelectric generator. Available from: < arXiv:1508.01153 > .
[19] Ebling D, Bartholomé K, Bartel M, Jägle M. Module geometry and contact resistance of thermoelectric generators analyzed by multiphysics simulation. J Electron Mater 2010;39(9):1376–80.
[20] Eriksson L. Mean value models for exhaust system temperatures. Tech rep. SAE Technical Paper; 2002.
[21] Aranguren P, Astrain D, Rodríguez A, Martínez A. Experimental investigation of the applicability of a thermoelectric generator to recover waste heat from a combustion chamber. Appl Energy 2015;152:121–30.
[22] Lazard M, Fraisse G, Goupil C, Scherrer H. Thermal analysis of a thermoelectric: a way to non conventional design. In: Proceedings of the 6th European conference on thermoelectrics, vol. 1; 2008. p. 2e15.
[23] Starr M, Buckingham J, Jackson C. Development of transient test cycles for selected nonroad diesel engines. ASME Int Combust Eng Div Publ ICE 1999;32:145–56.
[24] Dou D. Application of diesel oxidation catalyst and diesel particulate filter for diesel engine powered non-road machines. Platinum Met Rev 2012;56(3):144–54.